Research Article

pISSN 2799-8525 · eISSN 2799-8681
J Powder Mater 2025;32(2):95-103

Journal of
Powder Materials

# Ultra-Low-Temperature (4.2 K) Tensile Properties and Deformation Mechanism of Stainless Steel 304L Manufactured by Laser Powder Bed Fusion

**Seung-Min Jeon[1,2], Young-Sang Na[2], Young-Kyun Kim[2,*]**

[1]Department of Smart Manufacturing Engineering, Changwon National University, Changwon 51140, Republic of Korea
[2]Korea Institute of Materials Science, Changwon 51508, Republic of Korea

This study investigated the ultra-low-temperature (4.2 K) tensile properties and deformation mechanisms of stainless steel 304L manufactured via laser powder bed fusion (LPBF). The tensile properties of LPBF 304L were compared to those of conventional 304L to assess its suitability for cryogenic applications. The results revealed that LPBF 304L exhibited a significantly higher yield strength but lower ultimate tensile strength and elongation than conventional 304L at 4.2 K. The temperature dependence of the yield strength also favored LPBF 304L. Microstructural analysis demonstrated that LPBF 304L features a high density of dislocation cells and nano-inclusions, contributing to its greater strength. Furthermore, strain-induced martensitic transformation was observed as a key deformation mechanism at cryogenic temperatures, where austenite transformed into both hexagonal-closed packed (HCP) and body-centered cubic (BCC) martensite. Notably, BCC martensite nucleation occurred within a single HCP band. These findings provide critical insights into the mechanical behavior of LPBF 304L at cryogenic temperatures and its potential for applications in extreme environments.

**Keywords:** Laser powder bed fusion (LPBF); Stainless steel 304L; Extremely low temperature; Tensile properties; Microstructure

**Received:** February 20, 2025
**Revised:** April 7, 2025
**Accepted:** April 7, 2025

***Corresponding author:**
Young-Kyun Kim
E-mail: ykkim@kims.re.kr

## 1. Introduction

The hydrogen economy has emerged as a key alternative for reducing carbon emissions and mitigating greenhouse gases [1, 2]. With the increasing use of hydrogen in various sectors—including renewable energy, fuel cells, and the aerospace industry—the demand for materials that can perform reliably in hydrogen environments is expected to grow steadily [3-6]. In particular, liquid hydrogen ($LH_2$) has attracted significant attention due to its high gravity energy density (33.3 kWh/kg) and excellent storage efficiency compared to gaseous hydrogen. However, because $LH_2$ boils at −253 °C, it is imperative to evaluate the safety of materials intended for use in such ultralow temperature environments.

Metal additive manufacturing (MAM) technologies have revolutionized production by enabling the fabrication of geometrically complex components that are unattainable through traditional manufacturing methods [7, 8]. Among various materials used at cryogenic temperatures, 304L stainless steel (STS) is highly favored owing to its outstanding stability and mechanical properties under low-temperature conditions [9-12]. In particular, laser powder bed fusion (LPBF) utilizes a high-power laser to locally melt selected areas of metal powder. The rapid cooling and solidification in LPBF enable hetero-structuring and hierarchical microstructure. Moreover, the uniform thin-layer deposition—on the order of tens to hundreds of micrometers—allows for excellent mechanical properties to be achieved, provided that optimal process parameters are employed.

Despite these advantages, metallic materials fabricated via AM frequently exhibit notable microstructural defects such as porosity, dislocation network-induced substructure, texture, and oxide formation during AM [13-15]. While controlled mi-

https://doi.org/10.4150/jpm.2025.00066

crostructural defects can sometimes impart strengthening effects and enhance mechanical performance, excessive defects are detrimental to mechanical behavior of materials. This is particularly critical in ultralow temperature environments, where the primary carriers of dislocation glide may be restricted, and reduced phase stability can lead to phase transformations from face-centered cubic (FCC) to body-centered cubic (BCC) structure. Consequently, microstructural defects can have a more pronounced adverse effect on mechanical properties at cryogenic temperatures. Thus, it is essential to evaluate the performance of AM materials under these conditions before considering their application in cryogenic environments. In the present study, we address these challenges by investigating the tensile properties of LPBF-manufactured STS 304L at 4.2 K. We discuss the correlations between the microstructure and tensile properties and compare the performance with that of conventional commercial STS 304L to provide a comprehensive understanding of the potential of AM materials for cryogenic applications.

## 2. Experimental procedure

### 2.1. Materials

Table 1 shows the chemical compositions of LPBF 304L and conventional 304L, which were chosen for their similar compositions to facilitate a direct comparison of their microstructures and tensile properties. The chemical compositions of both LPBF and conventional stainless steels are based on the manufacturer's mill sheet specifications. The LPBF 304L was produced using gas-atomized AISI 304L powder with an average particle size of 37 μm. The metal 3D printer ProX DMP 300 from 3D Systems was employed for the LPBF process. This printer utilizes a continuous laser with a spot size of 100 μm and a 175 W laser beam that traverses the powder bed at a speed of 1000 mm/s. The laser scanning strategy involves a 90° rotation between successive layers, resulting in a rectangular specimen with dimensions of 90 mm × 23 mm × 5 mm.

### 2.2. Ultralow temperature (4.2 K) tensile testing

Ultralow temperature tensile tests were performed using a liquid helium tensile testing machine at the Korea Institute of Materials Science (KIMS) [16]. The system continuously supplies liquid helium to cool the specimen, and once the attached cryogenic temperature sensor stabilizes at 4.2 K, the tensile test is started. Dog-bone specimens with gauge dimensions of 12.0 × 3.0 × 1.2 $mm^3$ were fabricated in accordance with ASTM E8. The tensile tests were conducted at an initial strain rate of 1 × $10^{-3}s^{-1}$.

### 2.3. Microstructural observation

The microstructures were examined using a field-emission scanning electron microscope (FE-SEM; MIRA3, TESCAN) and an electron backscatter diffraction (EBSD) detector (Nordlys Nano, Oxford Instruments). EBSD images were collected under optimized conditions at an accelerating voltage of 20 kV and a working distance of 12 mm. In addition, the electron channeling contrast (ECC) technique was utilized to investigate dislocation structures, with ECC images acquired at 30 kV and a 7 mm working distance. For sample preparation, an automatic polisher (Dualprep 3-AP4, Allied) was used. All specimens were ground using silicon carbide papers (#400–#2000) and diamond suspensions with an average particle size of 1 μm, followed by a final polishing step with colloidal silica (average particle size of 0.04 μm).

## 3. Results and Discussion

### 3.1. Initial microstructure

Fig. 1 shows the initial microstructural characteristics of LPBF 304L (a-c) and conventional STS 304L (d-f), as revealed by inverse pole figure (IPF) maps, phase maps, and ECC images. The IPF map of LPBF 304L obtained from a plane perpendicular to the build direction reveals a grid-like grain structure with an average grain size of 31.6 μm (Fig. 1a). This grid pattern is characteristic of LPBF processes where the build direction rotates by 90° between successive layers [17, 18]. Notably, no δ-ferrite is detected in LPBF 304L, which is entirely austenitic (Fig. 1b). In contrast, the conventional 304L consists of equiaxed grains with a few annealing twins, exhibiting an average grain size of 58.7 μm (Fig. 1d). It predominantly comprises

**Table 1.** Chemical composition of conventional STS 304L and LPBF 304L powder. (wt. %)

| Wt % | Fe | Si | Mn | P | S | Cr | Ni | Mo | Co | N | C | O |
|---|---|---|---|---|---|---|---|---|---|---|---|---|
| Conventional STS 304L | Bal. | 0.45 | 1.67 | 0.031 | 0.002 | 18.21 | 8.06 | 0.14 | 0.21 | 0.14 | 0.028 | - |
| LPBF 304L powder | Bal. | 0.75 | 1.39 | 0.02 | 0.01 | 18.95 | 9.71 | - | - | 0.11 | 0.02 | 0.10 |

LPBF, laser powder bed fusion.

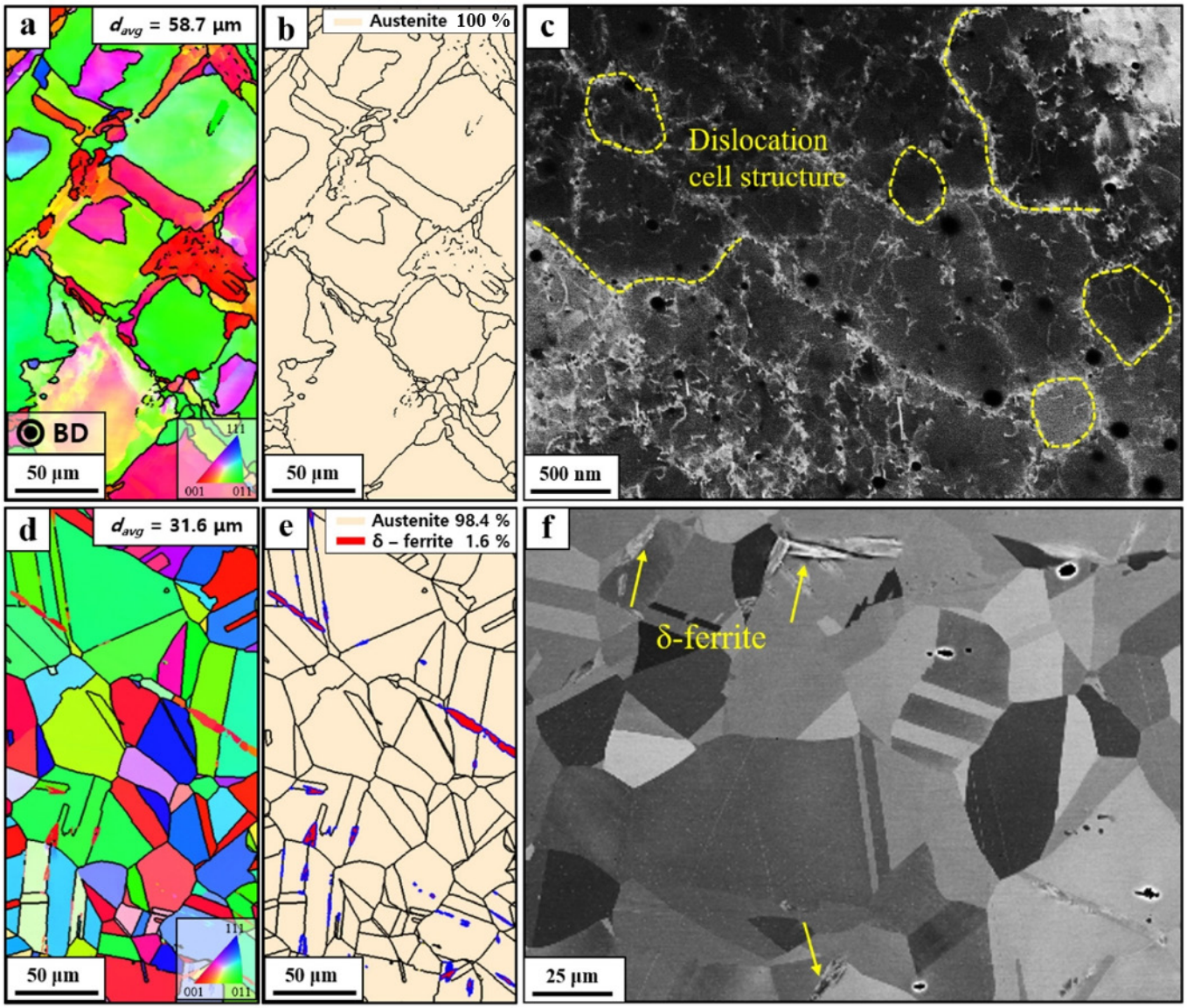


**Fig. 1.** (a, d) Electron backscatter diffusion inverse pole figure (IPF), (b, e) phase maps, (c, f) electron channeling contrast (ECC) image of (a-c) LPBF STS 304L and (d-f) conventional STS 304L indicating the initial microstructure. LPBF, laser powder bed fusion.

austenite, with a minor fraction (1.6%) of δ-ferrite observed (Fig. 1e).

Further insights into the microstructures were obtained through ECC analysis. As shown in Fig. 1c (LPBF 304L) and Fig. 1f (conventional 304L), the LPBF 304L exhibits a high density of dislocations arranged in a cellular structure. This dislocation cell structure likely results from the rapid solidification and repetitive thermal cycling inherent to the LPBF process, which generates and accumulates dislocations that subsequently arrange themselves to minimize the internal energy [19]. Additionally, small, dark oxide particles, which presumably formed during the LPBF process, are observed. Conversely, the ECC image of conventional 304L (Fig. 2e) shows a near absence of dislocations, with the equiaxed grains and δ-ferrite clearly visible in the IPF and phase maps.

Due to the nature of the LPBF process, the formation of oxides and porosity can occur during fabrication. During printing, the oxygen level in the chamber was maintained at approximately 0.2%. The as-received powder contained 106 ± 5 ppm of oxygen, which increased to 440 ± 12 ppm in the printed material. This 334 ppm increase suggests the formation of oxide particles within the SS304L matrix during processing. Oxygen content was measured using a LECO TC-436 nitrogen-oxygen analyzer. Porosity in conventional STS 304L is typically

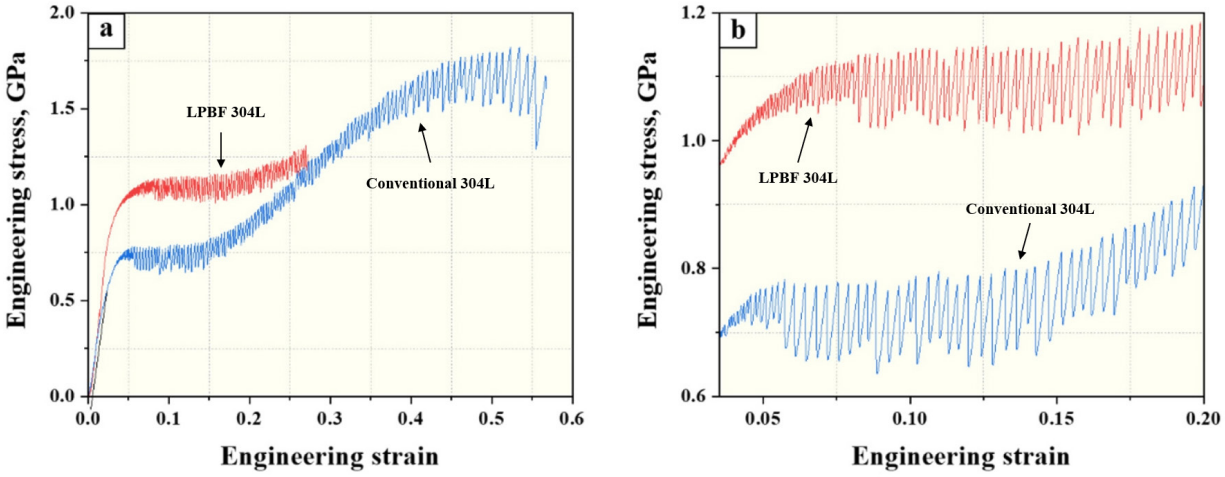


**Fig. 2.** (a) Engineering stress-strain curve at 4.2 K and (b) cropped image in (a) showing a different discontinuous plastic flow behavior of conventional 304L (blue line) and LPBF 304L (red line). LPBF, laser powder bed fusion.

negligible, owing to its homogeneous and densely compacted manufacturing process. In contrast, LPBF 304L exhibited a porosity of approximately 0.01%, as determined by micro-CT analysis using a Phoenix Vtomex M system from Waygate Technologies.

### 3.2. Ultralow temperature (4.2 K) tensile properties

Fig. 2a presents the tensile properties of LPBF 304L and conventional 304L in a liquid helium environment (4.2 K). At 4.2 K, conventional 304L exhibits a yield strength (YS) of 549.8 MPa, an ultimate tensile strength (UTS) of 1.81 GPa, and an elongation of 56.5%. In contrast, the LPBF-manufactured STS 304L shows a higher YS of 777.8 MPa, but a lower UTS of 1.31 GPa and an elongation of 27.5% compared to conventional 304L. Although the UTS and elongation of LPBF 304L are inferior, its yield strength exceeds that of conventional 304L by over 40%. This implies that LPBF 304L exhibits superior structural stability at cryogenic temperatures (i.e., liquid helium and/or liquid hydrogen) compared to conventional 304L, thereby facilitating the design of lighter metallic components.

Both materials display pronounced discontinuous plastic flow (DPF) phenomenon, characterized by load-drop in stress–strain curves. Such serrations with an unstable oscillation are typically attributed to dynamic strain aging (DSA) during deformation at intermediate temperatures [20]. However, at 4.2 K the thermal energy is insufficient to activate DSA, implying that alternative mechanisms must be responsible for the serrated behavior. Two prevailing models have been proposed:

1. Mechanical instability model: Seeger et al. [21] reported that dislocation interactions among different slip systems lead to the formation of Lomer-Cottrell (L-C) locks. At cryogenic temperatures, limited thermal activation causes dislocations to accumulate until the stress concentration reaches the theoretical shear strength, at which point a sudden collapse of the L–C locks results in a stress drop. Therefore, the sequential formation and collapse of these locks are considered to the origin of serration at extremely low temperatures.
2. Thermomechanical instability model: First proposed by Basinski [22], this model suggests that plastic deformation results in dislocation multiplication, which converts mechanical work into heat. Due to the very low specific heat at cryogenic temperatures, localized plastic deformation can lead to temperature spikes of several tens of Kelvin. This adiabatic heating lowers the flow stress locally, causing a sudden stress drop.

Although it is not definitively established which mechanism predominates, both models invoke the localized buildup and subsequent collapse of dislocations to explain the stress drops. Notably, as the strain increases, the serrations become more pronounced (Fig. 2b), and the magnitude of the stress drops grows. This is likely due to the enhanced accumulation of dislocations and L–C locks as the deformation proceeded. Although LPBF 304L exhibits roughly 40% higher yield strength, its stress drop is slightly lower, measuring at 120 MPa compared to 144 MPa for conventional 304L. This indicate that

LPBF 304L experiences fewer temperature spikes or a slower rate of dislocation generation and accumulation, and that differences in physical properties (e.g., the strength of local L–C locks or specific heat variations due to compositional differences) govern the extent of the stress drop.

### 3.3. Temperature dependence of yield strength for LPBF and conventional 304L

Fig. 3 illustrates the yield strengths of both conventional 304L and LPBF 304L as a function of temperature. In addition to the 4.2 K tests, tensile experiments were conducted at room temperature (298 K) and in liquid nitrogen (77 K) to assess temperature dependence. The yield strength data over these three temperatures were fitted with an exponential function from 4.2 K to 298 K, described by [23]:

$$\sigma_{Ys}(T) = \sigma_a \exp\left(-\frac{T}{C}\right) + \sigma_b \quad (1)$$

Where $\sigma_a$, $\sigma_b$, and $C$ are fitting constants. Here, $\sigma_a$ represents the thermal (temperature-dependent) component of yield strength, while $\sigma_b$ accounts for the temperature independent (athermal) part.

Table 2 presents the fitting constants for both conventional 304L and LPBF 304L. The results reveal that LPBF 304L has higher values for both the thermal-dependent fitting constant ($\sigma_a$) and athermal ($\sigma_b$) components compared to conventional 304L. In current alloys, the yield strength generally stems from the intrinsic lattice resistance to dislocation motion, referred to as the friction stress ($\Delta\sigma_{fr}$), combined with additional strengthening increments from multiple sources: the initial dislocation density ($\Delta\sigma_{dis}$), solid solution effects ($\Delta\sigma_{ss}$), precipitates ($\Delta\sigma_{fr}$), and grain boundary ($\Delta\sigma_{gb}$, via the Hall–Petch relationship). Hence, the yield strength can be expressed in a general form as:

$$\sigma_y = \sigma_{fr} + \Delta\sigma_{dis} + \Delta\sigma_{ss} + \Delta\sigma_{ppt} + \Delta\sigma_{gb} \quad (2)$$

Considering these strengthening components of yield strength, the higher athermal constant ($\sigma_b$) for LPBF 304L is due to the influence of $\sigma_{fr}$, $\Delta\sigma_{dis}$, $\Delta\sigma_{ppt}$, $\Delta\sigma_{gb}$. The influence of $\Delta\sigma_{ss}$ is negligible due to the little difference in composition between the two alloys. In LPBF 304L, we can see that the initial dislocation density is higher than conventional 304L, with a large number of dislocation cells (Fig. 1c and 1f). Additionally, nano inclusions, appearing as black dots, are widely distributed in large numbers. This distribution enhances the strengthening contributions of $\Delta\sigma_{dis}$ and $\Delta\sigma_{ppt}$. Furthermore, the friction stress $\sigma_{fr}$ increases due to the combined effects of the high initial dislocation density and the presence of nano inclusions, which enhance the intrinsic lattice resistance to dislocation motion. Consequently, even though the average grain size of LPBF 304L (58.7 μm) is larger than that of conventional 304L (31.6 μm)—thus granting conventional 304L a higher strengthning contribution from the Hall–Petch relationship—once the other strengthening factors are taken into account, the overall yield strength of LPBF 304L remains higher, as evidenced by the athermal constant ($\sigma_b$).

Thermal-dependent constant ($\sigma_a$) is also found to be higher in LPBF 304L, indicating a significant increment in yield strength as the temperature decreases. In this context, friction stress ($\sigma_{fr}$) plays a major role. Generally, friction stress is proportional to the magnitude of the Peierls-Nabarro barrier, which refers to the shear stress required to move dislocations through the crystal lattice along a specific direction. While the Peierls-Nabarro barrier is negligible in pure FCC metals, making them relatively insensitive to temperature changes, the material in this study exhibits increasing yield strength at cryogenic temperatures, suggesting a larger Peierls-Nabarro barrier.

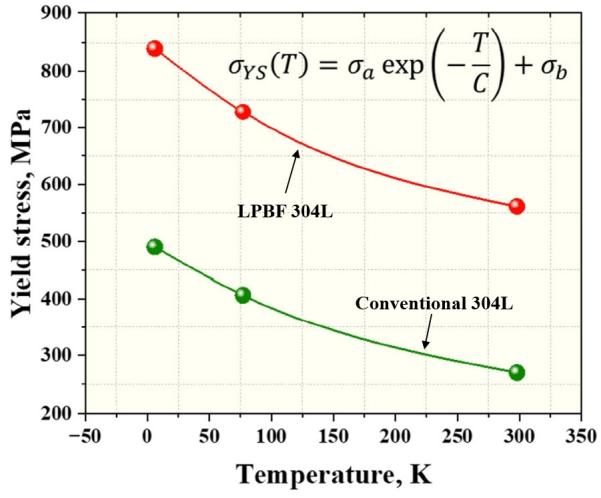


**Fig. 3.** Exponential function-fitted temperature dependence of the yield strength of conventional and LPBF 304L. LPBF, laser powder bed fusion.

**Table 2.** Fitting constants of the temperature dependence of yield strength for conventional and LPBF 304L

| | $\sigma_a$ (MPa) | $C$ | $\sigma_b$ (MPa) |
|---|---|---|---|
| Conventional 304L | 312.6 | 226.6 | 185.9 |
| LPBF 304L | 371.9 | 198.6 | 478.4 |

LPBF, laser powder bed fusion.

This can be attributed to the large number of dislocation cells and nano inclusions in LPBF 304L, which hinder dislocation movement and thus require greater activation energy, thereby increasing the Peierls-Nabarro barrier. At ultra-low temperatures, the available thermal energy to activate these dislocations is even more limited, so the Peierls-Nabarro barrier is expected to be larger still. Consequently, the yield strength increases further as the temperature decreases, and its temperature dependence also becomes more pronounced.

As a result, LPBF 304L has a higher initial dislocation density and contains more nano-inclusions, which leads to a higher thermal constant ($\sigma_b$) and thus a higher yield strength at room temperature. This also increases the Peierls-Nabarro barrier, thereby raising the temperature-dependent constant ($\sigma_a$) of the yield strength in LPBF 304L compared to conventional 304L.

### 3.4. Deformation behavior

Fig. 4 shows the deformed microstructure of LPBF 304L after tensile testing at 4.2 K. IPF map for the deformed specimen at 4.2 K reveals that the original grid-like grain structure evolved

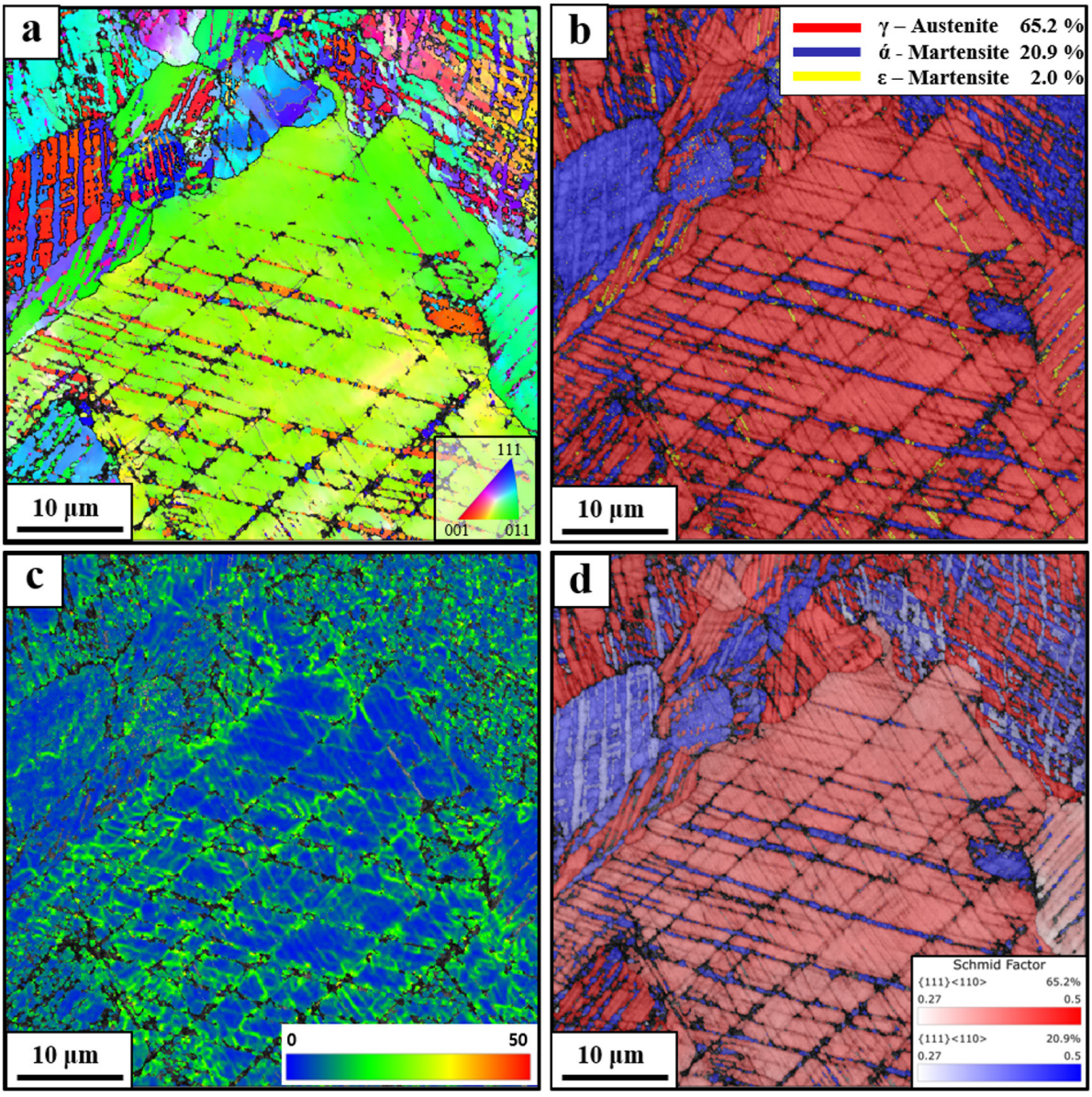


**Fig. 4.** 4.2 K Deformed microstructure of LPBF 304L. (a) Inverse pole figure (IPF) map, (b) phase map, (c) geometrically necessary dislocation (GND) map, (d) Schmid factor mapping (red: FCC phase, blue: BCC phase). LPBF, laser powder bed fusion; FCC, face-centered cubic; BCC, body-centered cubic.

into numerous deformation bands as strain was accommodated (Fig. 4a). In the phase map (Fig. 4b), these deformation bands are predominantly identified as the BCC phase, with a minor presence of the Hexagonal-closed packed (HCP) phase. It is worth noting that the volume fractions measured were 65.2% FCC, 20.9% BCC, and 2.0% HCP, respectively. These BCC bands are primarily generated by deformation and are indicative of strain-induced martensitic transformation (SIMT) [24, 25]. In stainless steels with low stacking fault energy (SFE), SIMT is known to alleviate strain concentration and promote more homogeneous deformation [26, 27]. Given that SIMT typically occurs in stainless steels with SFE in the range of 15–20 $mJ/m^2$ [27-29], it is evident that the primary deformation mechanism at 4.2 K in this material is the transformation to HCP or BCC martensite, facilitated by its low SFE. Fig. 4c presents a map of geometrically necessary dislocations (GNDs), revealing a substantial density of dislocations with an average GND density of $9.32 \times 10^{14}/m^2$. The GND density is notably higher near the BCC martensite regions, suggesting that the BCC martensite effectively impedes dislocation motion. Moreover, BCC martensite formed where the dislocations concentrated. Furthermore, the Schmid factor map (Fig. 4d) presents how well the external load (primarily in the tensile direction) is geometrically aligned with each grain's active slip system (or dislocation activity). A higher Schmid factor indicates that the slip system more readily contributes to deformation. SIMT at 4.2 K shows that it activates the slip system in the BCC region, which in turn relaxes the stress concentration in LPBF 304L, allowing for more uniform deformation.

To further elucidate the deformation mechanisms, ECCI analysis was performed on the deformed specimen at 4.2 K. Fig. 5 shows ECC images of a tensile fracture surface obtained at 4.2 K. Here, we present ECC images from a region exhibiting partial SIMT (a) and one predominantly undergoing SIMT (b). For the partial SIMT region (Fig. 5a), numerous dislocations and stacking faults are visible in FCC domain where SIMT has not yet occurred. In contrast, the region to the right of the dashed line is characterized by abundant HCP bands and localized BCC martensite formation. This observation is consistent with the EBSD results in Fig. 4 and clearly illustrates the evolution of dislocation behavior before and after SIMT. On the other hand, the ECC image reveals that LPBF 304L has a low SFE yet still retains some FCC domains. This outcome is likely due to the presence of numerous micro-defects, such as pores, in the additively manufactured material, which impede further progression of the SIMT and lead to premature fracture, leaving a portion of the FCC domains untransformed.

Fig. 5b provides a detailed view of the nucleation of BCC martensite, further corroborating the role of dislocation accumulation and SIMT in the deformation process. ECCI observations across multiple regions reveal that BCC martensite nucleates and grows via SIMT within a single HCP band. Although the exact nucleation sites of the fully developed martensitic regions cannot be identified, this transformation behavior differs from that typically observed in conventional STS under cryogenic conditions. it is generally reported that SIMT of STS results in BCC nucleation at the intersection of HCP bands [30, 31]. Ho et al. [30] and Kruml et al. [31] reported that at low

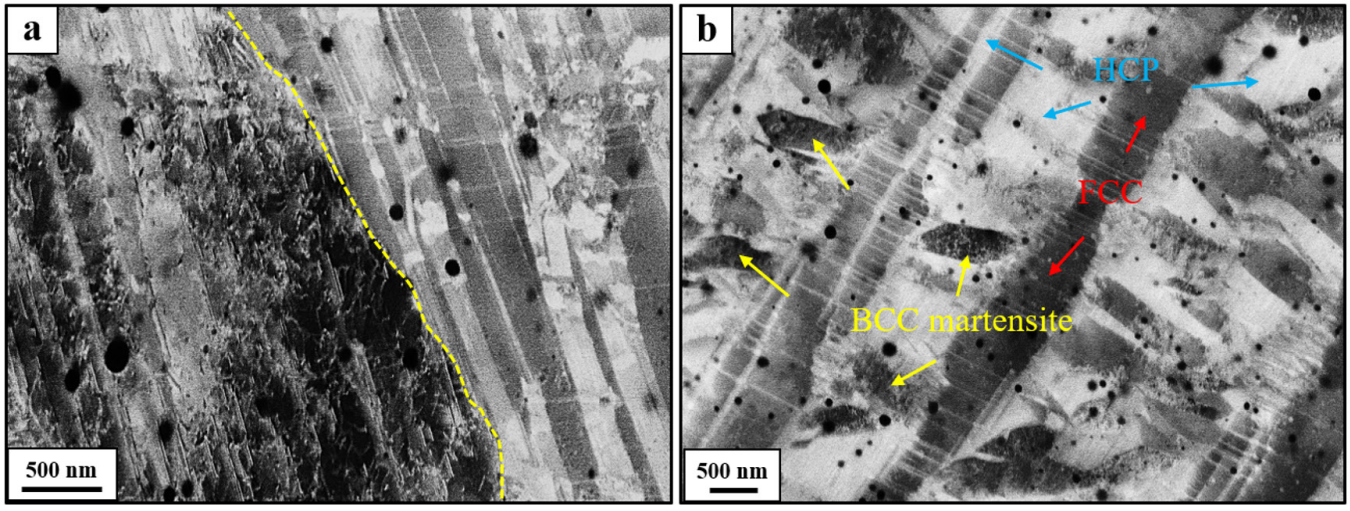


**Fig. 5.** Electron channeling contrast (ECC) image of a tensile sample deformed at 4.2 K showing (a) dislocation behavior and (b) strain-induced transformation.

temperatures, due to the low SFE, a perfect dislocation splits into two Shockley partial dislocations. The migration of these partial dislocations leads to the formation of HCP bands by introducing stacking fault. They also noted that the BCC martensite, which forms between two HCP bands, does not transform directly from austenite (FCC) to martensite (BCC). Instead, austenite first transforms into the energetically stable HCP phase, which then transitions into BCC martensite at the HCP band intersection. However, in the case of LPBF 304L, BCC nucleation occurred within a single HCP band, which differs from previous reports [30, 31]. This is likely due to the low activation energy for BCC martensite formation, which results from differences in the degree of activation of the slip system and austenite stability [32-34].

## 4. Conclusion

In this work, the ultra-low temperature (4.2 K) tensile properties and deformation mechanisms of stainless steel 304L manufactured via laser powder bed fusion (LPBF) were investigated. The summarized conclusions are as follows:

1. The LPBF-manufactured 304L exhibited a significantly higher yield strength at 4.2 K compared to conventional 304L. This enhancement is attributed to the high initial dislocation density and the presence of nano inclusions, which increase lattice resistance to dislocation motion.
2. The LPBF 304L exhibited a greater temperature dependence in yield strength compared to conventional 304L. The Peierls-Nabarro barrier, influenced by initial dislocation interactions and nano inclusions, contributed to this effect, highlighting the material's unique response to cryogenic conditions. In addition, a discontinuous plastic flow (DPF) was observed at 4.2 K, which was attributed to differences in the intrinsic physical properties.
3. Both HCP and BCC martensite phases were observed in the deformed microstructure, confirming that SIMT plays a critical role in the plastic deformation of LPBF 304L at 4.2 K. This transformation helps accommodate strain and contributes to mechanical stability under extreme conditions.
4. Unlike previous reports where BCC martensite nucleates at the intersection of HCP bands, this study observed BCC formation within single HCP bands in LPBF 304L. This distinct transformation pathway requires further investigation to fully understand its implications on mechanical behavior.
5. The superior yield strength and deformation characteristics of LPBF 304L indicate its potential for applications in cryogenic environments, such as hydrogen storage and aerospace structures. However, its reduced ductility and susceptibility to microstructural defects must be carefully considered in design and processing.

## Funding

This study was supported financially by Fundamental Research Program of the Korea Institute of Materials Science (No. PNKA320); and the Nano Material Technology Development Program (No. RS-2024-00445038) through the National Research Foundation of Korea).

## Conflict of Interest

The authors declare no competing financial interests or personal relationships.

## Data Availability Statement

The data that support the findings of this study are available from the corresponding author upon reasonable request.

## Author Information and Contribution

S.-M. Jeon: Investigation, Methodology, Writing – original draft. Y.-S. Na: Writing – review & editing, Supervision. Y.-K. Kim: Investigation, Methodology, Writing – original draft, Writing – review & editing, Supervision, Conceptualization.

## Acknowledgments

None.

## References

[1] S. Griffiths, B. K. Sovacool, J. Kim, M. Bazilian and J. M. Uratani: Energy Res. Soc. Sci., **80** (2021) 102208.
[2] T. Zhang, J. Uratani, Y. Huang, L. Xu, S. Griffiths and Y. Ding: Renewable Sustainable Energy Rev., **176** (2023) 113204.
[3] D. Kang, S. Yun and B. Kim: Energies, **15** (2022) 4357.
[4] M. Aziz: Energies, **14** (2021) 5917.
[5] J. Fesmire, A. Swanger, J. Jacobson and W. Notardonato:

IOP Conf. Ser.: Mater. Sci. Eng., **1240** (2022) 012088.
[6] L. Yin, H. Yang and Y. Ju: Int. J. Hydrog. Energy, **57** (2024) 1302.
[7] D. Herzog, V. Seyda, E. Wycisk and C. Emmelmann: Acta Mater., **117** (2016) 371.
[8] B. H. Jared, M. A. Aguilo, L. L. Beghini, B. L. Boyce, B. W. Clark, A. Cook, B. J. Kaehr and J. Robbins: Scr. Mater., **135** (2017) 141.
[9] T. DebRoy, H. L. Wei, J. S. Zuback, T. Mukherjee, J. W. Elmer, J. O. Milewski, A. M. Beese, A. Wilson-Heid, A. De and W. Zhang: Prog. Mater. Sci., **92** (2018) 112.
[10] C. Zheng and W. Yu: Mater. Sci. Eng. A, **710** (2018) 359.
[11] M. S. Kim, T. Lee, J. W. Part and Y. Kim: Metals, **13** (2023) 1774.
[12] T. Sakurai, O. Umezawa and Y. Ono: IOP Conf. Ser.: Mater. Sci. Eng., **1302** (2024) 012002.
[13] S. Chowdhury, N. Yadaiah, C. Prakash, S. Ramakrishna, S. Dixit, L. R. Gupta and D. Buddhi: J. Mater. Res. Technol., **20** (2022) 2109.
[14] S. R. Narasimharaju, W. Zeng, T. L. See, P. Scott, X. Jiang and S. Lou: J. Manuf. Processes, **75** (2022) 375.
[15] W. H. Kan, L. N. S. Chiu, C. V. S. Lim, Y. Zhu, Y. Tian, D. Jiang and A. Huang: J. Mater. Sci., **57** (2022) 9818.
[16] Y.-K. Kim, K.-R. Lim and Y-S. Na: Korean J. Met. Mater., **61** (2023) 389.
[17] N. Nadammal, T. Mishurova, T. Frisch, I. Serrano-Munoz, A. Kromm, C. Haberland, P. D. Portella and G. Bruno: Addit. Manuf., **38** (2021) 101792.
[18] B. Dovgyy, A. Piglione, P. A. Hooper and M. S. Pham: Mater. Des., **194** (2020) 108845.
[19] X. He, X. K. Shang, J. He and B. B. He: Mater. Charact., **217** (2024) 114335.
[20] S.-Y. Lee, C. Takushima, J.-I. Hamada and N. Nakada: Acta Mater., **205** (2021) 116560.
[21] A. Seeger, J. Diehl, S. Mader and H. Rebstock: Phil. Mag., **2** (1957) 323.
[22] Z. S. Basinski: Proc. R. Soc. London, Ser. A, **240** (1957) 229.
[23] Z. Wu, H. Bei, G. M. Pharr and E. P. George: Acta Mater., **81** (2014) 428.
[24] Y. F. Shena, X. X. Li, X. Sunb, Y. D. Wanga and L. Zuo: Mater. Sci. Eng. A, **552** (2012) 514.
[25] D. Molnar, X. Sun, S. Lu, W. Li, G. Engberg and L. Vitos: Mater. Sci. Eng. A, **759** (2019) 490.
[26] N. J. Simon and R. P. Reed: J. Nucl. Mater., **141-143** (1986) 44.
[27] S. Martin, S. Wolf, U. Martin, L. Krüger and D. Rafaja: Metall. Mater. Trans. A, **47** (2016) 49.
[28] L. Remy and A. Pineau: Mater. Sci. Eng., **28** (1977) 99.
[29] K. Sato, M. Ichinose, Y. Hirotsu and Y. Inoue: ISIJ Int., **29** (1989) 868.
[30] K. H. Lo, C. H. Shek and J. K. L. Lai: Mater. Sci. Eng.: R: Rep., **65** (2009) 39.
[31] T. Kruml, J. Polak and S. Degallaix: Mater. Sci. Eng. A, **293** (2000) 275.
[32] X.-S. Yang, S. Sun and T.-Y. Zhang: Acta Mater., **95** (2015) 264.
[33] Y. Tian, O. I. Gorbatov, A. Borgenstam, A. V. Ruban and P. Hedstrom: Metall. Mater. Trans. A, **48** (2017) 1.
[34] B. Wang, C. Hong, G. Winther, T. L. Christiansen and M. A. J. Somers: Mater., **12** (2020) 100751.